Experimental Analysis of a Degraded Open-Cathode PEM Fuel Cell Stack

Stephan Strahl[1,*], Noemí Gasamans[1,2], Jordi Llorca[2], Attila Husar[1]

[1] Institut de Robòtica i Informàtica Industrial (UPC/CSIC), C/ Llorens i Artigas 4, 08028 Barcelona, Spain

[2] Institut de Tècniques Energètiques, Universitat Politècnica de Catalunya, Av. Diagonal 647, 08028 Barcelona, Spain

[*] Corresponding author, sstrahl@iri.upc.edu

ABSTRACT

The well-known challenges to overcome in PEM fuel cell research are their relatively low durability and the high costs for the platinum catalysts. This work focuses on degradation mechanisms that are present in open-cathode PEM fuel cell systems and their links to the decaying fuel cell performance. Therefore a degraded, open-cathode, 20 cell, PEM fuel cell stack was analyzed by means of in-situ and ex-situ techniques. Voltage transients during external perturbations, such as changing temperature, humidity and stoichiometry show that degradation affects individual cells quite differently towards the end of life of the stack. Cells located close to the endplates of the stack show the biggest performance decay. Electrochemical impedance spectroscopy (EIS) data present non-reversible catalyst layer degradation but negligible membrane degradation of several cells. Post-mortem, ex-situ experiments, such as cyclic voltammetry (CV), X-ray photoelectron spectroscopy (XPS) and X-ray diffraction (XRD) show a significant active area loss of the first cells within the stack due to Pt dissolution, oxidation and agglomeration. Scanning electron microscopy (SEM) images of the degraded cells in comparison with the normally working cells in the stack show severe carbon corrosion of the cathode catalyst layers.

Keywords: PEMFC, Open-cathode, Degradation, in-situ and ex-situ experiments

1. INTRODUCTION

Although many applications have been developed for the past few years, PEM fuel cells must still meet or exceed the technological advantages, such as system lifetime and cost, of heat engines or other conventional power systems in order to be truly competitive. Thus, current research has to be focused on improving those aspects. Several government programs have been established in order to overcome the difficulties of market introduction for fuel cell systems. For example, the targets for durability of the U.S. Office of Energy Efficiency and Renewable Energy (EERE) are 5000 h for transportation by 2017 and 60000 h for stationary application by 2020 with less than 10% voltage decay over the lifetime of the system [1]. However, at present in most fuel cell systems this decay is already reached after around a thousand hours of operation [2], which makes the durability of cells and components one of the greatest technological challenges at the moment. PEM fuel cell lifetime is reduced among others by long operation at high potentials, power and subsequent thermal cycling or by operation incidents such as reactants starvation, contamination or inadequate water management [3-6].

In order to achieve the durability goals the EERE sets special targets for the individual cell components, such as membrane durability at voltage cycling, loss of electrochemical surface area (ECSA) of the catalyst layer, bipolar plate corrosion, etc. For example, the membrane must be capable of maintaining its performance with less than 5% loss from beginning to end of life without external humidification for transport applications [3]. Therefore, proper water management strategies are highly important research objectives. Yousefi-Steiner et al. [7] presented the importance of water management effects on reversible voltage degradation and possible irreversible fuel cell degradation. Lin et al. [8] performed in-situ and ex-situ experiments of a single PEM fuel cell during and after load cycling with humidified reactants. These experiments revealed severe structural and electrochemical changes within catalyst layer and membrane, which were responsible for significant performance degradation after 280h of operation. Guilminot et al. [9] investigated physical and chemical changes of PEM fuel cells after 529h operation at constant power. Their results show pronounced

changes in Pt distribution inside the MEA related to corrosion of the carbon support, Pt dissolution and crystallite growth.
Since external reactant humidification should be avoided because of additional cost, weight and power consumption, the study of degradation mechanisms of self-humidified, open-cathode systems, that do not require external humidification, is of great interest. In this context, in-situ and ex-situ analysis of an already degraded open-cathode stack can improve the comprehension of the related physical phenomena and lead to the development of control strategies in order to increase the fuel cell's durability.
A benefit of this work is that only few experimental data on the degradation of stacks, such as the work of Luo et al. [10], are available, especially if the effects are different from cell to cell. The objective of this work is the investigation, identification and separation of degradation phenomena that occur in the different parts of the membrane-electrode-assembly (MEA) of cells within an open-cathode PEM fuel cell stack.

2. EXPERIMENTAL ANALYSIS

2.1 Fuel cell system specifications

The system under observation in this work is the commercially available 100 W, 20 cell PEM fuel cell stack H-100 from Horizon Fuel Cells Technologies. This open-cathode system with an active area of 22.5 cm^2 is self-humidified and air-cooled. It includes a single cooling fan directly attached to the fuel cell housing, which removes heat from the stack by forced convection and at the same time provides oxygen to the cathode. Thus, the cathode air supply and the stack cooling cannot be decoupled. However, even the minimum cathode flow rate guarantees a stoichiometry of about 20 at the rated electrical power of 100 W. The anode inlet is supplied with dry hydrogen and the outlet features a purge valve for dead-ended operation and periodic purging. For testing under different ambient conditions, the stack is installed in an environmental chamber with the capability of controlling relative humidity, temperature and oxygen concentration of the ambient air.

2.2 Performance loss during lifetime

The stack was tested under the laboratory conditions shown in Table 1 within 1 year (February 2010 – March 2011). Experiments that have been conducted include EIS, Current Interrupt, Polarization Curves, as well as anode and cathode humidification studies and diffusion tests with nitrogen. The test station featured large anode inlet and outlet volumes that were not purged regularly with nitrogen after shutdown. In this period the stack was operated for approximately 280 h and underwent about 60 start-up/shutdown cycles. A notable voltage decay in cell 1 and 2 was observed, especially towards the end of the testing period.
From April 2011 to December 2012 the stack was installed in a demonstration plant and was run for about 20 h without data acquisition. Severe performance decay was detected when even the constant 60 W power demand of the demonstration plant could not be reached anymore. This was declared to be the end of life for the fuel cell. Before taking the stack apart for an ex-situ physical-chemical analysis, it was installed back into the test station for final in-situ experiments. The comparison of selected individual cell voltages at the beginning and end of life is shown in Figure 1. The voltages of cell 1 and 2 dropped to zero when applying a current higher than 2.5 A. All cells that are not shown in Figure 1 showed similar voltages as cell 9 and 10, which were therefore chosen as the reference cells for all the following experiments. Figure 1 shows that the first cells (cell 1 and 2) and at the last cell (cell 20) of the stack have been suffered from much high degradation rates than the rest of the cells. The anode reactant inlet and outlet are located at the endplate next to cell 1. The following sections try to elucidate the reasons for the severe degradation of cells within the stack by in-situ and ex-situ analysis.

2.3 In-situ experiments

2.3.1. Sensitivity to operating conditions

The in-situ experiments can deliver important data for detecting the degraded cells in the stack and for finding indicators for the respective type of degradation they suffered during operation. The dynamic cell voltage responses with respect to changes in stack current, ambient relative humidity and oxygen concentration were analyzed. LabVIEW data acquisition software was used in conjunction with the National Instruments Analog Input Module for Fuel Cells NI-9206 to measure the stack and single cell voltages. The

stack current was measured with a Chauvin Arnoux E3N current clamp. Vaisala HMM211 humidity sensors measured the anode and cathode inlet and outlet dew point temperatures.

2.3.2. Electrochemical Impedance Spectroscopy (EIS)

In order to separate the performance losses into membrane and catalyst related losses, EIS of the stack and single cells were carried out. EIS were performed using the Agilent 35670A Dynamic Signal Analyzer in conjunction with the electronic load TDI RBL488. The spectroscopies were carried out at a current density of 0.044 A cm^{-2} (I = 1 A) and ambient conditions of 25 ºC and 73% RH. The low current density was chosen since the huge voltage swing of the degraded cells during the spectroscopy at higher current densities led to non-representative impedance data. The frequency of the sinusoidal current perturbation signal was varied from 0.1 Hz to 10 kHz using an amplitude of 2.5 % of the current set point.

2.4 Ex-situ experiments

Once the in-situ experiments were finished and the data were analyzed, the stack was taken apart for ex-situ analysis. Comparative degradation characterization experiments of the cells with the lowest performance (cells 1, 2, and 20) were performed, taking normally working cells (cells 9, 10) as a reference. Figure 2 shows the anode side of an extracted membrane-electrode-assembly (MEA). The holes on the left and right of the MEA are part of the hydrogen inlet and outlet manifold that traverses the whole stack. The samples that have been taken for the different experiments from each analyzed cell are marked in red. For analysis of the anode and cathode catalyst layers (CL), the inner circle was cut out and the MEA was separated into anode, membrane and cathode at the respective catalyst-membrane-interfaces. The circle measures 25 mm in diameter for the CV experiments. The MEA was separated by immersion for 5 min in a 1:1 (w/w) water:isopropanol mixture in an ultrasonic bath, according to the procedure presented by Danerol et al. [11]. Since the catalyst ink is applied to the gas diffusion layer (GDL), the membrane detaches after a few minutes in the ultrasonic bath from both CLs, which remained attached to the GDLs.

2.4.1 Cyclic voltammetry (CV)

The loss of electrochemical active surface area (ECSA) relative to a reference cell (cell 9) of the analyzed anode and cathode CLs was determined by CV (0-0.5 V) with an Autolab PGSTAT100N galvanostat. The CLs were mounted in a three-electrode electrochemical cell with an Ag/AgCl reference electrode and a Pt counter electrode. Sulfuric acid (0.5 M) was used as the proton source. For obtaining a good CV response signal with well pronounced hydrogen desorption peaks, several tests at different sweep rates from 5 to 50 mV s^{-1} were performed for anode and cathode CLs. Based on these preliminary tests the optimal sweep rate for all anodes was set to 0.02 V s^{-1} and for all cathodes to 0.005 V s^{-1}. The ECSA is obtained by identifying the hydrogen desorption peak and integrating the current over the time passed under the peak.

2.4.2 X-ray diffraction (XRD) analysis

Pt particle growth due to Ostwald ripening may significantly decrease the ECSA. XRD analysis was carried out in order to compare the Pt particle size of the analyzed anode and cathode CLs. XRD patterns were collected between 10 and 90° of 2θ with a step width of 0.02° and a step time of 1 s using a Bruker D8 instrument equipped with Cu Kα incident radiation (λ=1.5404 Å) and a graphite monochromator.

2.4.3 X-ray photoelectron spectroscopy (XPS) analysis

The oxidation of Pt in the CLs leads to significant ECSA loss. In order to assess the Pt oxidation state of the analyzed anode and cathode CLs, surface characterization was carried out with XPS on a SPECS system. The system is equipped with an Al anode XR50 source operating at 150 mW and a Phoibos 150 MCD-9 detector. The pressure in the analysis chamber was below 10^{-7} Pa. The area analyzed was about 0.5 x 0.5 cm^2. The pass energy of the hemispherical analyzer was set to 25 eV with a step width of 0.1 eV. The binding energy (BE) values were referred to the C 1s peak at 284.8 eV.

2.4.4 Scanning electron microscope (SEM) investigations

The microstructure, morphology, and composition of the separated CL surfaces were studied with SEM. A Zeiss NEON40 crossbeam microscope operated at 10 kV and equipped with energy dispersive X-ray analysis (EDX), secondary electron, backscattered electron and in-lens detectors was employed. The morphology of the different layers within the MEA was studied in sections close to the anode inlet and

outlet, as depicted in Figure 2. Pieces of 0.5 x 2.5 cm^2 were cut out of the studied MEAs at the specified section in Figure 2, embedded in epoxy resin and polished for SEM observation.

3. RESULTS AND DISCUSSION

3.1 In-situ experiments

For the sake of clarity not all cell voltages of the 20 cells are plotted in the following figures of the in-situ experiments. Instead, only those that show a different behavior compared to the rest of the cells (e.g. cell 2) are depicted. Cell 9 is plotted in order to represent the rest of the cells, which all show a similar dynamic response to the applied perturbations.

3.1.1. Effect of cathode humidity

Figure 3 shows the changes in the voltages of cells 1, 2 and 9 while changing the ambient conditions from 20 ºC / 23 % RH to 25 ºC / 73 % RH (represented by the ambient dew point temperature) via an environmental chamber. Once the current increases from 1 to 2 A, cell voltage 2 almost drops down to 0 V. However, when increasing cathode humidification the cell recovers slightly. Finally voltage spikes appear which result from oxygen injections into the environmental chamber in order to maintain a homogeneous ambient oxygen concentration. The oxygen concentration oscillates continuously in saw tooth shape about +/- 0.05 % around a set point of 20.8 %. Even though the oxygen injections are present in the same form under dry ambient conditions (23 % RH), the voltage spikes cannot be observed. Hence, this behavior represents the activation of otherwise not active catalyst sites due to presence of a higher liquid water content in the cathode catalyst layer, as described in [12]. This phenomenon is only present in cell 2, which indicates that advanced catalyst layer degradation occurred in this cell.

3.1.2. Effect of cathode stoichiometry

The effect of higher cathode stoichiometry on the degraded cells was tested by increasing the oxygen content of the ambient air in the environmental chamber. Figure 4 shows how an increase of the oxygen set point from 20.8 % to 21.3% manages to stabilize the voltage of cell 2. As explained in section 3.1.1, part of the active area of cell 2 is degraded. The cathode catalyst layer may have suffered from carbon corrosion during start-up/shut-down cycles, as well as during long operation at open-circuit-voltage (OCV). This leads to a loss of the carbon support structure and agglomeration of the Pt particles [12]. However, by improving the reaction at non-degraded active sites through humidification and an increased cathode stoichiometry, the cell voltage may partly be recovered, as shown in Figure 4.

3.1.3. Analysis of impedance data

Figure 5(a) shows the Nyquist plot of the impedance data of the first 3 cells of the stack compared to a normally-working cell (9) in the middle and the last cell (20) at a current density of 0.044 A cm^{-2} and ambient conditions of 25ºC / 73% RH. All other cells of the stack that are not represented in Figure 5 show similar impedance data as cell 9. As depicted in Figure 5(a) all Nyquist semicircles are depressed, which is a common observation in most fuel cells because of in-homogeneous electrochemical reaction sites, spatial distribution of physical parameters and thus an imperfect double layer capacity [13].

Cell 2 shows the biggest low frequency arc, followed by cell 1 and 3. The Faradaic resistance R_f, which is represented by the difference between low frequency resistance (R_{LF}) and high frequency resistance (R_{HF}), increased more than 3 times during lifetime in cell 2 compared to cell 9. R_f gives information about the reaction kinetics of the electrochemical interface of the cathode CL rather than the anode CL due to the sluggish reaction kinetics of the oxygen reduction reaction [14].

The phase plots of the individual cells shown in Figure 5(b) are expected to be identical if the only change in the system is a variation of the active surface due to different operating conditions, such as the state of hydration of the cell [12]. Since all cells in the stack, besides cell 2, show a similar phase diagram as cell 9 we assume a significant change in the dielectric properties of the double-layer capacity of cell 2, caused by morphological changes in the cathode CL. Thus, this performance loss is due to non-reversible degradation mechanisms, such as a loss of ECSA, instead of just possible lack of humidification in the catalyst layer. A similar performance loss has been detected by Lin et al. [8] for a single cell after 280 h of dynamic load cycling, resulting from severe loss of ECSA.

Degradation of the membrane is represented by an increase in the membrane resistance, which is approximately equivalent to the cells' R_{HF}. Figure 5(c) shows that cell 1 and 2 feature elevated membrane resistances compared to the rest of the cells. However, the change in membrane resistance is negligible compared to the huge differences in the low frequency resistance, shown in Figure 5(a). In contrast to the results obtained by Lin et al. [8] after load cycling, severe membrane degradation can already be excluded here. However, the EIS data of Lin et al. [8] also do not show significant membrane degradation up to 280h of operation, just as the results presented in Figure 5(a). Only after continuation of the driving cycle experiment up to 370h a significant increase of the high frequency resistance could be observed in [8].

3.1.4. Discussion of in-situ results

Summarizing the results of the sensitivity experiments and the EIS data would lead to the assumption that the degradation of the stack started at cell 1 and 2, and has already been affecting cell 3, so far. However, also cell 20 shows similar degradation effects in the Nyquist and Bode diagrams, as well as an elevated membrane resistance. Thus, a hypothesis to be proved by ex-situ analysis of the stack under study is that degradation is more severe in cells close the endplates, especially in the first cells, which are next to the anode gas inlet and outlet. However, at the end of life, cell 2 presents the worst performance in all in-situ experiments, which will be further discussed in the following ex-situ analysis sections.

The analysis of the extracted in-situ data shows that the cathode catalyst layers of cells 1 and 2 have suffered severe degradation. This led to a significant loss in ECSA of these cells, compared to normally working cells in the middle of the stack.

3.2 Ex-situ experiments

The conclusions and hypothesis of the in-situ analysis were evaluated by a comparative physical and chemical ex-situ examination of cells 1, 2, 9, 10 and 20. Similar to the in-situ experiments, cells 9 and 10 have been considered as normally working reference cells.

3.2.1. Comparative ECSA analysis with CV

Figure 6 shows the comparison of the cyclic voltammograms of the analyzed anode (Figure 6a) and cathode (Figure 6b) CLs. The cathodes of cells 9, 10 and 20 show normal behaviour, presenting the typical hydrogen adsorption and desorption peaks for the polycrystalline Pt catalyst [9]. At voltages between 0.3 V and 0.5 V only the double layer contributes to the shape of the voltammogram. The voltammograms of the cathodes of cells 1 and 2 hardly show any active area at all, since only the capacitive charging current contribution is captured by the CV. Figure 6a shows that all tested anodes besides cell 20 present similar voltammograms.

Table 2 summarizes the relative values of ECSA for the anode and cathode CLs taking the cell 9 as the reference for both anode and cathode CLs. The relative ECSA values represent the deviation from the reference cell. Table 2 shows that the ECSA of the cathodes of cells 1 and 2 is almost completely lost which coincides with the very poor performance of these cells in the in-situ experiments. Another interesting result of the anode CVs is the lower ECSA of cell 20. The reasons for the loss of active area are investigated by XRD, XPS and SEM experiments. As shown by the anode voltammograms in Figure 6a, the anode CL of cell 9 does not perform best which results in positive percentages relative to cell 9.

3.2.2. Pt particle size analysis with XRD

The XRD analysis permits the characterization of Pt particle growth that may have occurred in the different cells due to Ostwald ripening. Figure 7 shows the XRD patterns of the cathode CLs of cells 1, 2, 9 and 10. The pattern of cell 9 matches perfectly with cell 10, which explains the similar results of the CV and the similar performance in the in-situ experiments. The sharpening of the Pt(111) diffraction peak is evident for the degraded cathodes, which indicates a considerable increase in the volume-averaged crystal size of Pt [15] in cells 1 and 2. The average platinum crystal sizes of the CL samples were estimated using the Scherrer equation [16] and matching the experimental data with a Gaussian distribution pattern. However, the patterns of cells 1 and 2 do not follow a Gaussian distribution, which results from the presence of two different Pt particle sizes. Therefore, the sum of two Gaussian distribution patterns have been used for the estimation of the particle sizes of cells 1 and 2, assuming that the smaller particle size of the two is similar to the determined Pt particle sizes of cell 9 and 10. The resulting Pt particle sizes of the different anode and cathode CLs are summarized in Table 3.

The analysis of the anode CLs did not show any differences in the XRD patterns neither in the determined Pt particle sizes of the different cells. The anode of cell 1 and the cathode of cell 20 were not analyzed in order to limit the number of experiments. The cathode CLs of cells 1 and 2 show the presence of Pt particles that are 3 to 4 times bigger than the particles in cells 9 and 10. However, cells 9 and 10 also show Pt particle growth, assuming that a pristine CL features particle sizes of 2-3 nm [15]. This is a result of Ostwald ripening due to high cathode potentials [3], which may be a result of long OCV operation and uncontrolled start-ups and shutdowns due to the formation of air/fuel boundary at the anode [17]. During high potential phases close to 1V or even higher during start-up and shutdown, Pt dissolves at the cathode, diffuses and redeposits on larger particles in order to reduce their surface energy. This may lead to a 50 % loss in ECSA [3].

3.2.3. Pt oxidation analysis with XPS

In order to analyze if part of the detected ECSA loss is due to oxidation of Pt, surface characterization of the cathode CLs was carried out with XPS. Figure 8 shows the Pt spectra of the cathodes of cells 1, 2 and 9, corresponding to the Pt 4f core level. The presence of Pt in the XPS spectra is indicated by photoelectrons originating in the 4f orbital, which results in a doublet due to the spin-orbit coupling [18], corresponding to the $4f_{7/2}$ and $4f_{5/2}$ levels. The accurate deconvolution of the spectra yields in all cases two doublet peaks, which indicate the existence of two different Pt oxidation states. The lower binding energy values of 70.7-71.1 eV and 74.1-74.4 eV (red) are assigned to metallic Pt ($4f_{7/2}$ and $4f_{5/2}$ levels, respectively), in accordance to values reported in the literature [19,20], while the doublet of oxidized Pt shows peaks at 73.6-74.1 eV and 76.6-77.3 eV corresponding to the $4f_{7/2}$ and $4f_{5/2}$ levels, respectively (blue). By comparison of the binding energy values of oxidized Pt to the values reported in the literature [20,21], oxidized Pt likely corresponds to PtO. The observed differences in binding energy values for the different cells are not significant and may arise for slightly different charging phenomena. Comparison of the XPS spectra of cells 1 and 2 with cell 9 demonstrates an increase in the percentage of oxidized Pt from 25% in cell 9 to 71% and 80% in cells 1 and 2, respectively. Therefore, the large amount of oxidized Pt may explain the very high relative ECSA loss of cells 1 and 2 determined by CV, as presented in section 3.2.1. In fact, it has been reported that Pt oxidation and the subsequent dissolution into the ionomer is intensified by operation at high cathode potentials, e.g. during long OCV operation [3]. Moreover, experiments of Uchimura et al. [22] have shown that Pt dissolution is also boosted by load cycling due to the creation and adsorption of oxides. The experiments showed that the loss in electrochemically active surface area and activity are the highest for cycling at the widest potential span. Since in the case of the studied stack voltage cycling has not been performed during its lifetime, the determined amount of oxidized Pt is attributed to long abidance at high potentials.

3.2.4. Morphological analysis with SEM

The CL surfaces were studied with SEM in order to analyze morphological and structural changes. Figure 9 shows the SEM images of the cathode CLs of cells 2 and 9 at a magnification factor of 1000 and 50000, as well as the anode CLs of cells 9 and 20 at a magnification factor of 50000. The electrochemical changes in activity, as observed in the previous experiments, are easily detected by SEM analysis of the CLs. Comparing the CLs of cells 2 and 9 at low magnification shows the increased amount of cracks in the catalyst layer. The high magnification images differ in the morphology of the carbon/ionomer mixture. The CL of cell 2 features less structural carbon support and a more inhomogeneous distribution of the ionomer with respect to the carbon support particles. This is the result of more severe carbon corrosion in the cathode of cell 2. The comparison of the anode CLs of cells 9 and 20 also depicts changes in the morphology that may explain the lower relative ECSA of cell 20, shown in Table 2. Since cell 20 is the last cell in the stack with respect to the hydrogen inlet, it is the first that suffers from possible hydrogen starvation situations. Hydrogen starvation may occur between anode purges, when the system is operated in the dead-ended mode. Especially the cooler cells that are located at the endplates are affected because of the higher liquid water content compared to warmer cells in the middle of the stack. The starvation events cause local voltage reversal, which in turn causes corrosion of the anode carbon support and the resulting performance decay [23].

The images of the cut MEA samples in epoxy are presented in Figure 10. The comparison of cells 9 and 2 shows severe carbon corrosion effects in the cathode CL of cell 2. Especially at the outlet of cell 2 the support degradation led to gaps between the membrane and the CL, which explains the very bad performance of this cell. SEM images of Cell 1 showed similar results.

In conclusion, the cathode CLs of the first cells in the stack show the strongest CL degradation, especially towards the anode outlet of each cell. This can be explained by the formation of an air/hydrogen boundary by diffusion of air into the anode outlet during uncontrolled start-up or shutdown of the system, which creates regions with different potentials [24]. The cathode CL close to the anode outlet may experience a potential of about twice that of OCV, which makes the carbon support corrode quickly in that region. Corrosion causes support structure decay, which leads to Pt dissolution and agglomeration and thus decreases the ECSA, as observed in the CV experiments. A similar post-mortem analysis of Tang et al. [17] revealed a reduction of the cathode catalyst layer thickness by about 66% after 80 corrosion cycles.
Carbon corrosion at start-up and shutdown can be mitigated by reactant and voltage control via nitrogen purges and voltage limitation (shorting resistor), for instance. However, in the studied system these mitigation actions were not applied, which led to severe carbon corrosion already after 60 start/stop cycles.
Comparing the in-situ results after humidification, as discussed in section 3.1.1, with the SEM images of cell 2 may explain the voltage behavior. The lost proton conductivity between ionomer and degraded Pt sites can partially be recovered by humidification of the cathode CL. Liquid water in water-filled agglomerates of the CL provides the necessary proton conduction path [25] which was lost due to carbon corrosion.
Finally, Pt migration and subsequent precipitation in the ionomer via reduction by the crossover hydrogen from the anode can be observed in all tested cells.

3.2.5. Discussion of ex-situ results

The presented ex-situ results show that the cells at the beginning (cells 1 and 2) and at the end of the stack (cell 20) suffered from higher degradation rates than cells in the middle of the stack (cells 9 and 10). Especially the first cells show the largest ECSA loss relative to cell 9, which is the result of severe carbon corrosion due to their location close to the anode inlet and outlet of the stack. The corrosion of the carbon support led to Pt dissolution, agglomeration and migration, which were detected by XPS, XRD and SEM analysis. The transversal SEM analysis of the first cells compared to cell 9 supports the hypothesis, that cells located close the anode gas inlet and outlet suffer first from carbon corrosion, in accordance with the post-mortem analysis results presented by Tang et al. [17]. Therefore the performance decay due to non-reversible CL degradation was first detected in cell 1 and advanced towards cell 3, until reaching almost complete loss of ECSA of the first two cells, while the rest of the stack was still operating reasonably well. This leads to the conclusion, that the uncontrolled start-ups and shutdowns had the strongest effect on the stack's durability.
The performance difference between cell 1 and cell 2, observed in the in-situ experiments, is via ex-situ analysis only noticeable in the XPS results and slightly in the XRD spectra. Reasons for the worse performance of cell 2 may be MEA and manufacturing process deviations.
A critical factor is that the test station featured large anode inlet and outlet volumes for hydrogen supply into the environmental chamber to the stack and the exhaust from the laboratory. Since the tubing was not purged regularly with nitrogen after shutdown, the cathode stayed at high potential after shutdown. Once air starts to diffuse into the anode outlet carbon corrosion rates increase, especially in the cathodes of the first cells, which explains the strong degradation of the first cells. The result is the severe ECSA loss of cell 1 and 2, compared to the moderate ECSA loss determined by Lin et al. [8] after 280h of load cycling.
In order to reduce high potentials and the corrosion effects, nitrogen purging after shutdown is important. Moreover, the anode inlet and outlet volumes have to be minimized by placing the inlet and outlet valves of the test station as close as possible to the studied stack.

4. CONCLUSIONS

An experimental in-situ and ex-situ study has been performed on a degraded, 20 cell, open-cathode PEM fuel cell stack. Single cell voltage data shows that cells located next to the endplates of the stack suffered much more degradation than cells in the middle of the stack. EIS analysis indicates non-reversible catalyst layer degradation. Observation of voltage transients during changes of cathode humidification as well as cathode stoichiometry shows a distinctive sensitivity of the degraded cells, which indicates a reduction of available active sites. A comparative ex-situ analysis of the worst and best cells in the stack, consisting of CV, XRD, XPS and SEM, resulted in a significant ECSA loss of the cathode CLs of the first cells of the stack. The reasons for the determined loss of ECSA are Pt oxidation and dissolution in the ionomer, Pt particle growth and Pt agglomeration. These phenomena mainly resulted from carbon corrosion of the cathode catalyst support structure during uncontrolled start-up and shutdown procedures. This work shows the low durability of an apart from that simple and robust open-cathode PEM fuel cell system. The durability of the system can

be improved significantly by proper start-up/shutdown control, avoidance of OCV operation and proper thermal and water management. The identification of the different degradation mechanisms in this work provides important knowledge in order to improve operating conditions and to design proper system controllers that take into account fuel cell durability.

5. ACKNOWLEDGEMENTS

The in-situ experiments were performed at the Fuel Cells Laboratory of the Institut de Robòtica i Informàtica Industrial (CSIC-UPC, Barcelona). XRD, XPS and SEM experiments were carried out at the hydrogen laboratory of the Institute of Energy Technologies (UPC, Barcelona). CV experiments were performed at the Laboratory of Electrochemistry of Materials and Environment (UB, Barcelona). Special thanks go to Prof. Pere Cabot for enabling and supporting the CV experiments. All experiments were only possible due to the laboratories' advanced equipment and proficient technical staff. This work is partially funded by the national projects MICINN DPI2011-25649 and MINECO ENE2012-36368, as well as by the 7th Framework Programme of the European Commission in the context of the Fuel Cells and Hydrogen Joint Undertaking (FCH JU) through the project PUMA-MIND FP7 303419.

REFERENCES

1. EERE. U.S. Department of Energy: Office of Energy Efficiency and Renewable Energy. http://www1.eere.energy.gov/hydrogenandfuelcells/mypp/, August 2013.
2. Wang, Y., Chen, K. S., Mishler, J., Cho, S. C., Adroher, X. C. (2011). A review of polymer electrolyte membrane fuel cells: Technology, applications, and needs on fundamental research. *Applied Energy*, *88*(4), 981-1007.
3. Mench, Matthew M., Emin Caglan Kumbur, and T. Nejat Veziroglu. *Polymer electrolyte fuel cell degradation*. Academic Press, 2011.
4. Wu, J., Yuan, X. Z., Martin, J. J., Wang, H., Zhang, J., Shen, J., Wu, S., et al. (2008). A review of PEM fuel cell durability: Degradation mechanisms and mitigation strategies. *Journal of Power Sources*, *184*(1), 104–119.
5. Schmittinger, W., Vahidi, A. (2008). A review of the main parameters influencing long-term performance and durability of PEM fuel cells. *Journal of Power Sources*, *180*(1), 1-14.
6. Cheng, X., Shi, Z., Glass, N., Zhang, L., Zhang, J., Song, D., Shen, J. (2007). A review of PEM hydrogen fuel cell contamination: Impacts, mechanisms, and mitigation. *Journal of Power Sources*, *165*(2), 739-756.
7. Yousfi-Steiner, N., Moçotéguy, P., Candusso, D., Hissel, D., Hernandez, A., Aslanides, A. (2008). A review on PEM voltage degradation associated with water management: Impacts, influent factors and characterization. *Journal of Power Sources*, *183*(1), 260-274.
8. Lin, R., Li, B., Hou, Y. P., Ma, J. M. (2009). Investigation of dynamic driving cycle effect on performance degradation and microstructure change of PEM fuel cell. *International Journal of Hydrogen Energy*, *34*(5), 2369-2376.
9. Guilminot, E., Corcella, A., Charlot, F., Maillard, F., Chatenet, M. (2007). Detection of Pt z+ ions and Pt nanoparticles inside the membrane of a used PEMFC. *Journal of The Electrochemical Society*, *154*(1), B96-B105.
10. Luo, Z., Li, D., Tang, H., Pan, M., & Ruan, R. (2006). Degradation behavior of membrane–electrode-assembly materials in 10-cell PEMFC stack. *International journal of hydrogen energy*, *31*(13), 1831-1837.
11. Danerol, A. S., Bas, C., Flandin, L., Claude, E., Alberola, N. D. (2011). Influence of ageing in fuel cell on membrane/electrodes interfaces. *Journal of Power Sources*, *196*(7), 3479-3484.
12. M. Ciureanu. Effects of Nafion dehydration in PEM fuel cells. *Journal of Applied Electrochemistry*, vol. 34, pages 705-714, 2004.
13. Fouquet, N., Doulet, C., Nouillant, C., Dauphin-Tanguy, G., Ould-Bouamama, B. (2006). Model based PEM fuel cell state-of-health monitoring via ac impedance measurements. *Journal of Power Sources*, *159*(2), 905–913.
14. R. O'Hayre, S. Cha, W. Colella, F.B. Prinz. *Fuel cell fundamentals*. John Wiley & Sons Inc., 2009.
15. Ferreira, P. J., Shao-Horn, Y., Morgan, D., Makharia, R., Kocha, S., Gasteiger, H. A. (2005). Instability of Pt/C Electrocatalysts in Proton Exchange Membrane Fuel Cells A Mechanistic Investigation. *Journal of The Electrochemical Society*, *152*(11), A2256-A2271.

16. Whiston, C., Prichard, F. E. *X-ray Methods*. John Wiley & Sons Inc., 1987.
17. Tang, H., Qi, Z., Ramani, M., Elter, J. F. (2006). PEM fuel cell cathode carbon corrosion due to the formation of air/fuel boundary at the anode. *Journal of Power Sources*, *158*(2), 1306-1312.
18. Zhang, F. Y., Advani, S. G., Prasad, A. K., Boggs, M. E., Sullivan, S. P., Beebe Jr, T. P. (2009). Quantitative characterization of catalyst layer degradation in PEM fuel cells by X-ray photoelectron spectroscopy. *Electrochimica Acta*, *54*(16), 4025-4030.
19. Thiele, J., Barrett, N. T., Belkhou, R., Guillot, C., Koundi, H. (1994). An experimental study of the growth of Co/Pt (111) by core level photoemission spectroscopy, low-energy electron diffraction and Auger electron spectroscopy. *Journal of Physics: Condensed Matter*, *6*(27), 5025.
20. Kim, K. S., Winograd, N., Davis, R. E. (1971). Electron spectroscopy of platinum-oxygen surfaces and application to electrochemical studies. *Journal of the American Chemical Society*, *93*(23), 6296-6297.
21. Drawdy, J. E., Hoflund, G. B., Gardner, S. D., Yngvadottir, E., Schryer, D. R. (1990). Effect of pretreatment on a platinized tin oxide catalyst used for low-temperature Co oxidation. *Surface and Interface Analysis*, *16*(1-12), 369-374.
22. M. Uchimura, S. Sugawara, Y. Suzuki, J. Zhang and S.S. Kocha (2008). Electrocatalyst Durability under Simulated Automotive Drive Cycles. ECS Transactions 16(2), 225–234.
23. Ferreira-Aparicio, P., Chaparro, A. M., Gallardo, B., Folgado, M. A., Daza, L. (2010). Anode degradation effects in PEMFC stacks by localized fuel starvation. *ECS Transactions*, *26*(1), 257-265.
24. Reiser, C. A., Bregoli, L., Patterson, T. W., Jung, S. Y., Yang, J. D., Perry, M. L., Jarvi, T. D. (2005). A reverse-current decay mechanism for fuel cells. *Electrochemical and Solid-State Letters*, *8*(6), A273-A276.
25. Wang, Q., Eikerling, M., Song, D., Liu, Z. (2004). Structure and performance of different types of agglomerates in cathode catalyst layers of PEM fuel cells. *Journal of Electroanalytical Chemistry*, *573*(1), 61-69.

FIGURES

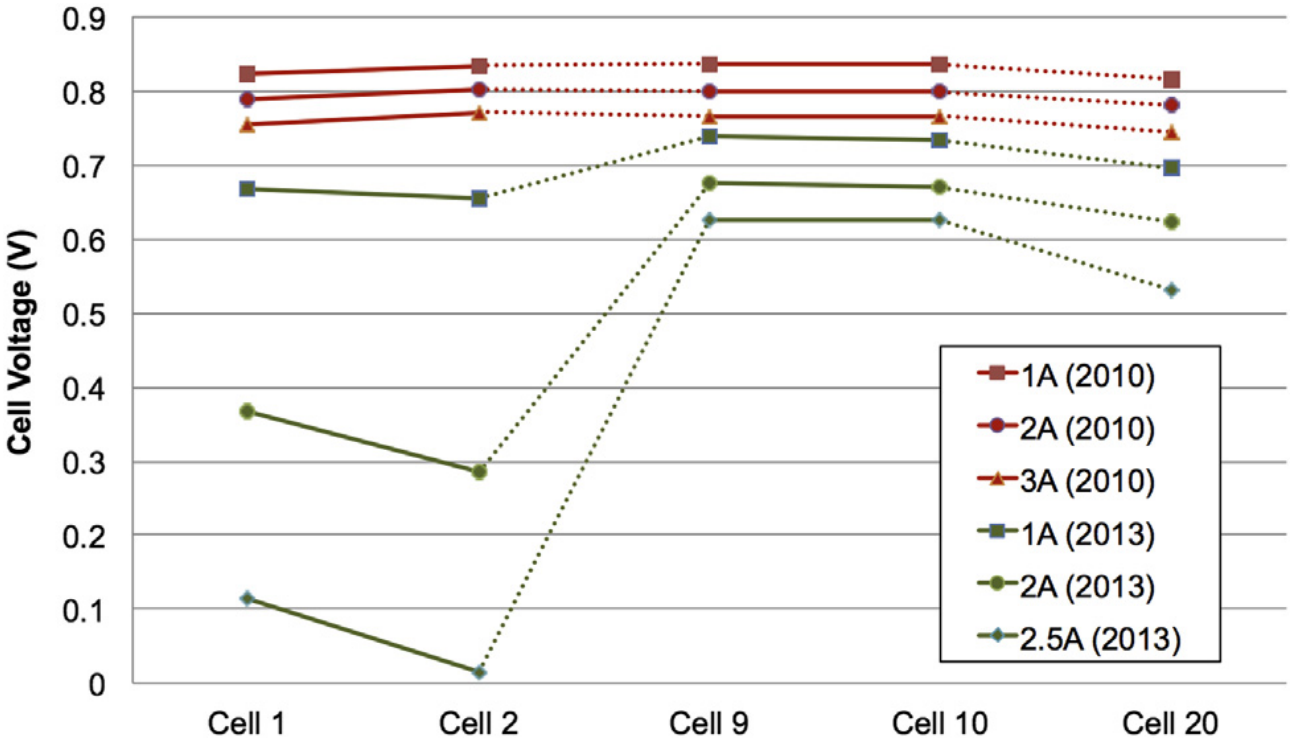

Figure 1: Comparison of selected cell voltages at beginning and end of life and at different stack currents (Active area = 22.5 cm^2).

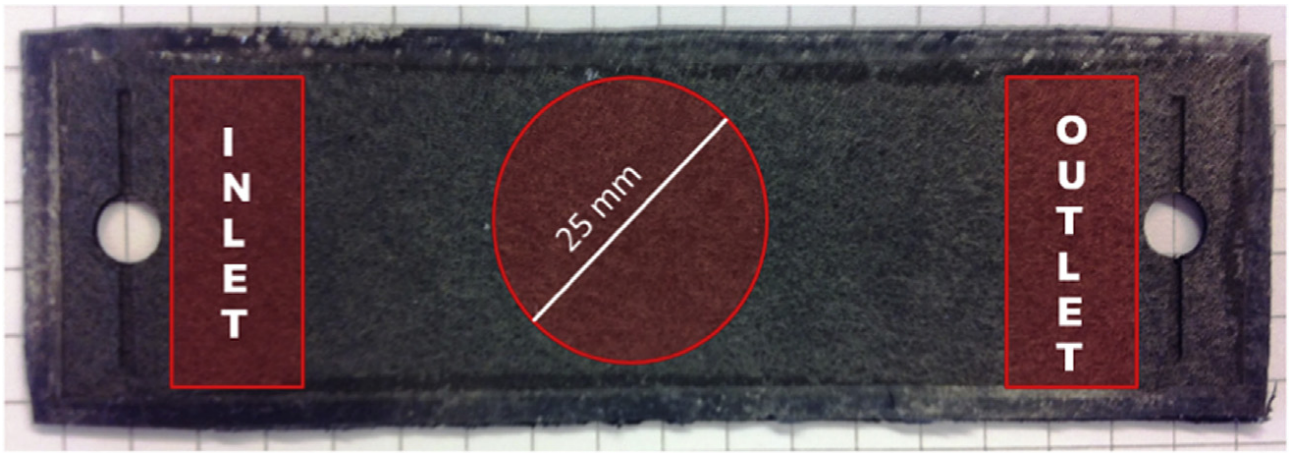

Figure 2: Anode side of an extracted MEA from the stack. The zones for taking samples for the ex-situ experiments are marked in red.

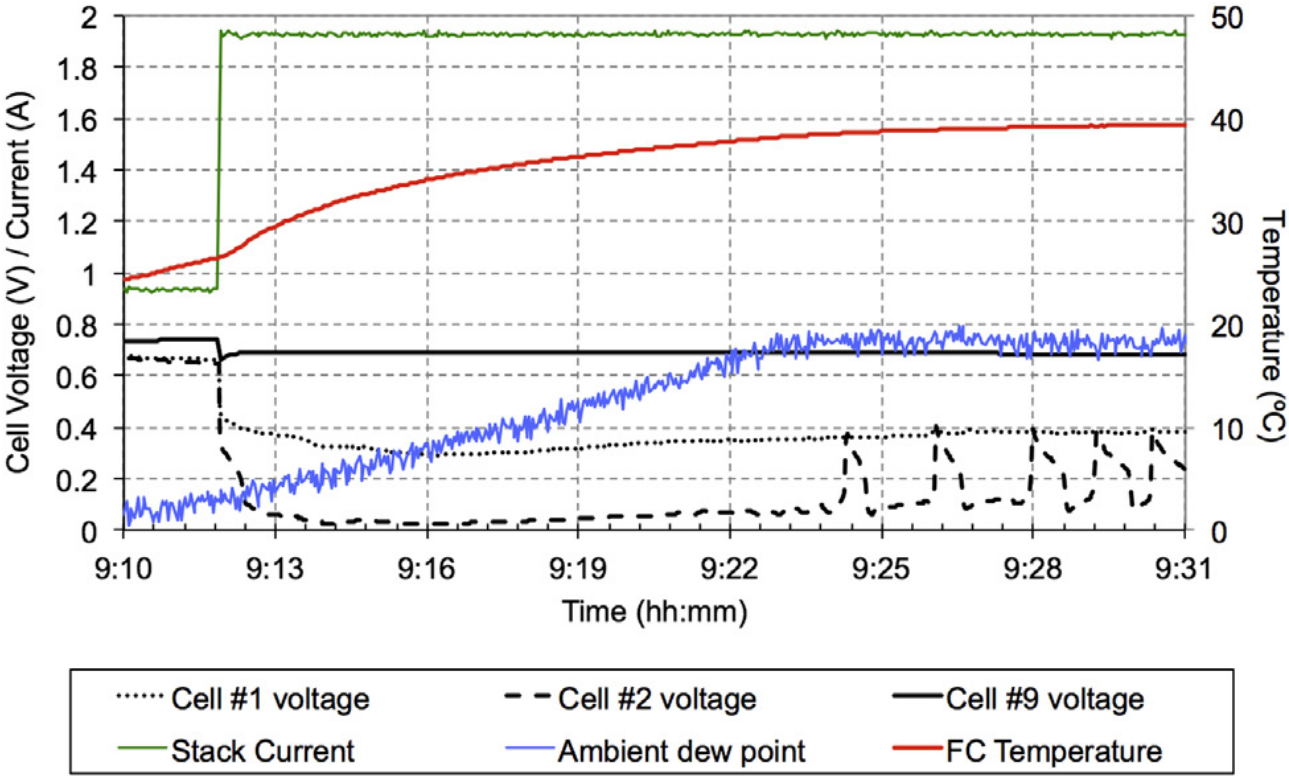

Figure 3: Selected cell voltages, stack current, stack temperature and ambient dew point temperature during humidification of the ambient air from 23 to 73 % RH.

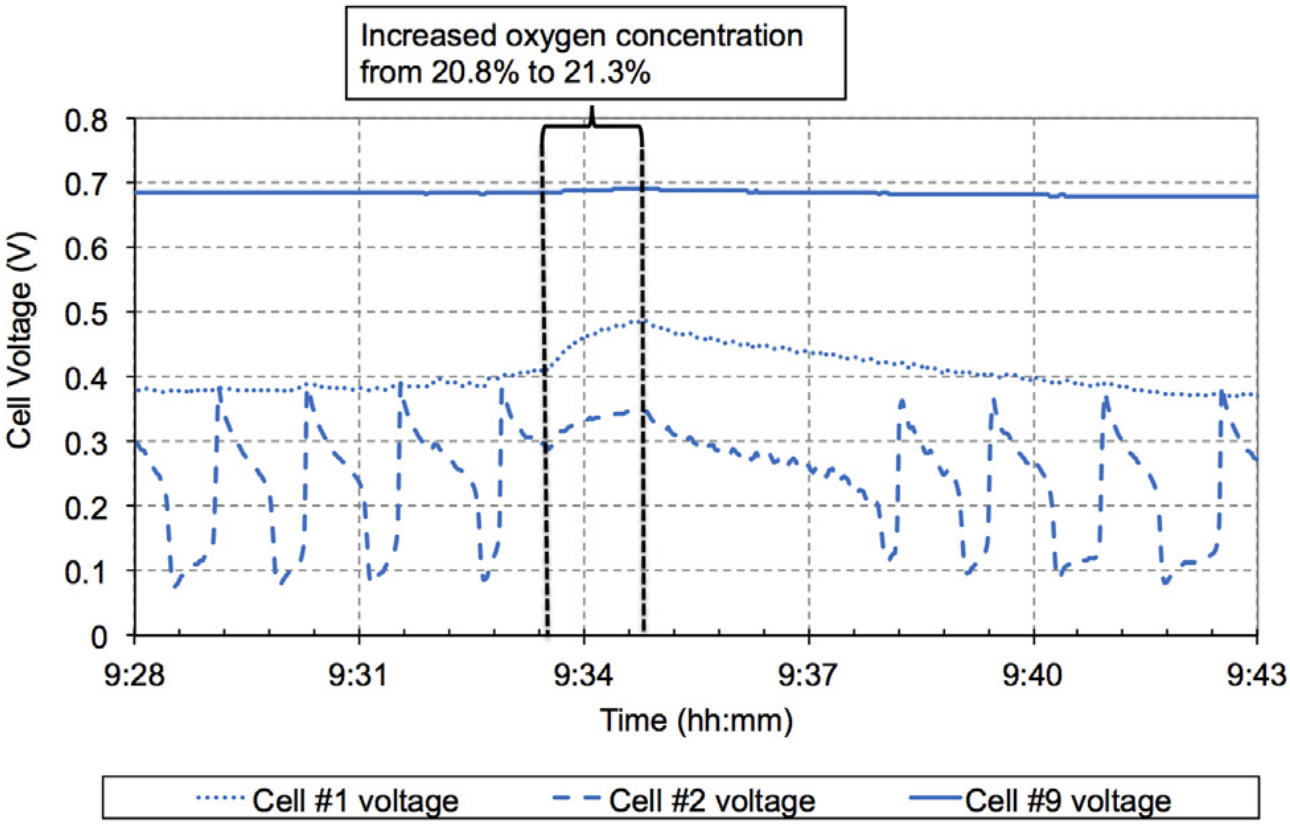

Figure 4: Selected cell voltages during a change in ambient oxygen concentration from 20.8% to 21.3%.

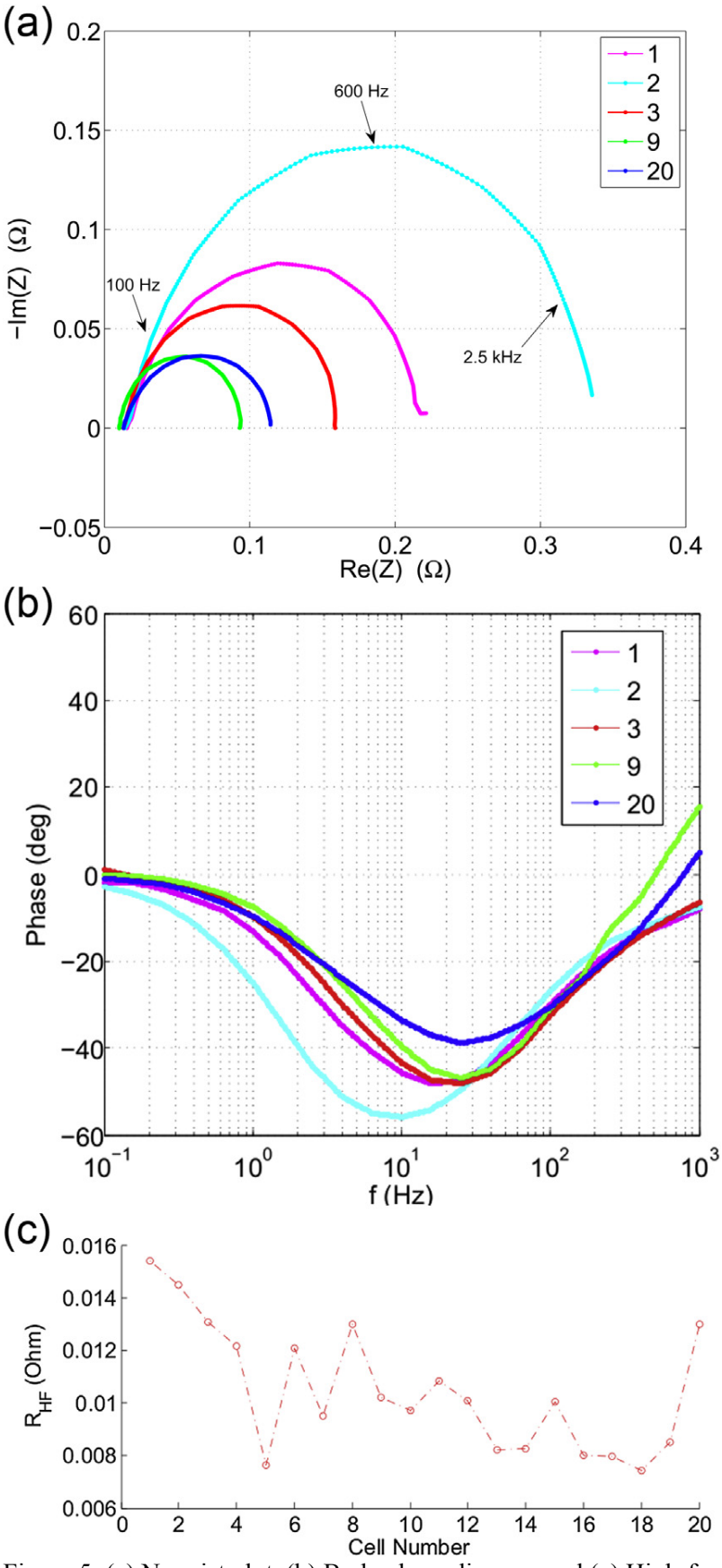

Figure 5: (a) Nyquist plot, (b) Bode phase diagram and (c) High-frequency resistance of selected cells at a current density of 0.044 A cm^2 and 25ºC / 73 % RH ambient conditions.

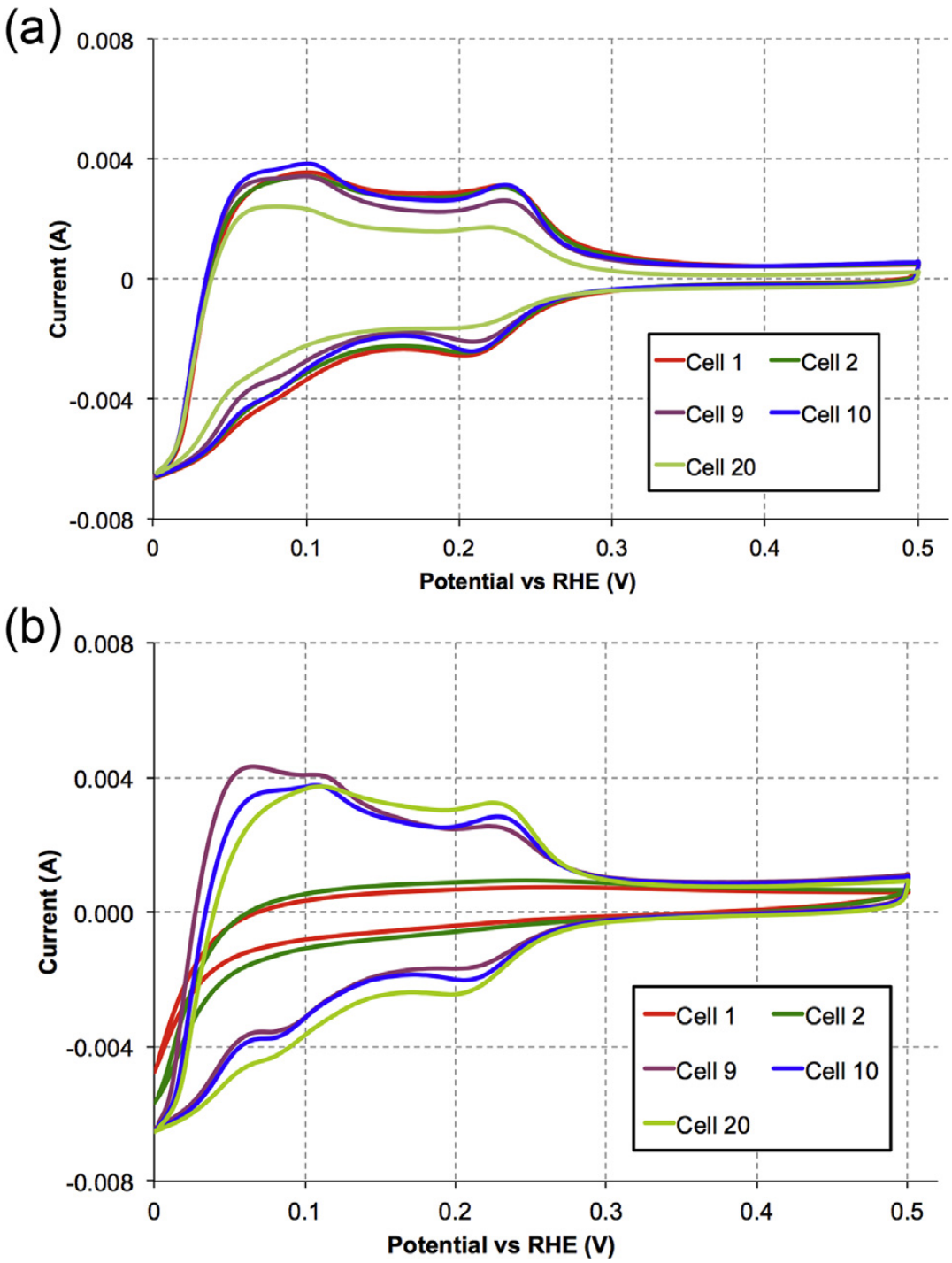

Figure 6: Voltammograms of (a) anode and (b) cathode CLs of selected cells as results of CV from 0-0.5 V with a sweep rate of 0.02 V s^{-1} and 0.005 V s^{-1}, respectively.

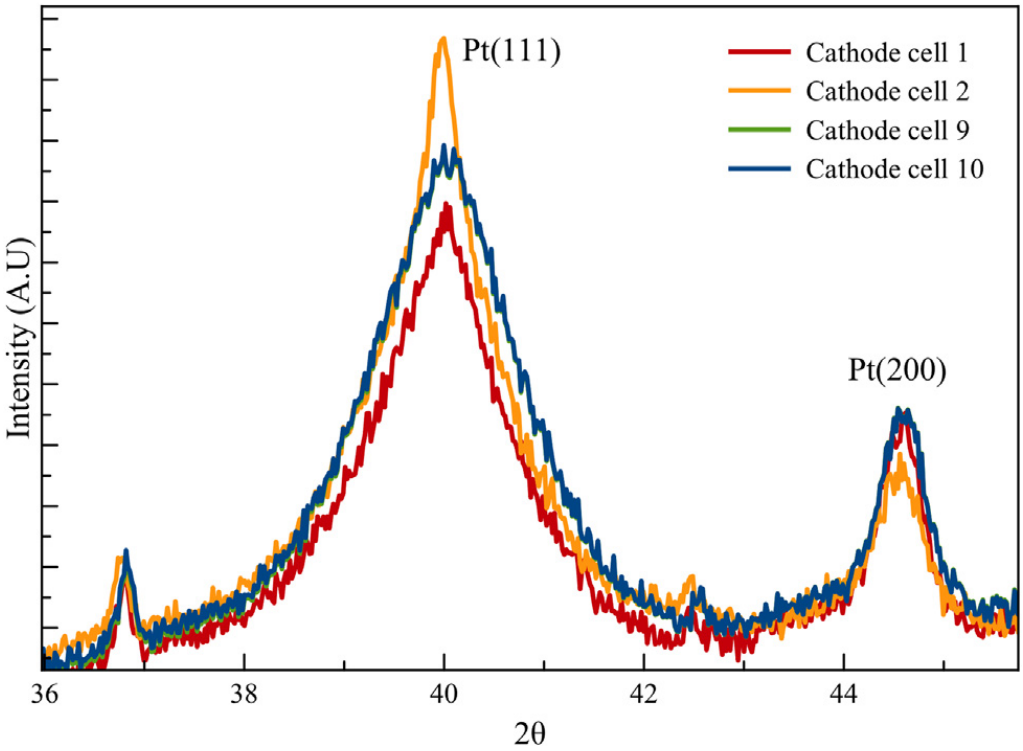

Figure 7: XRD patterns of the cathode CLs of selected cells.

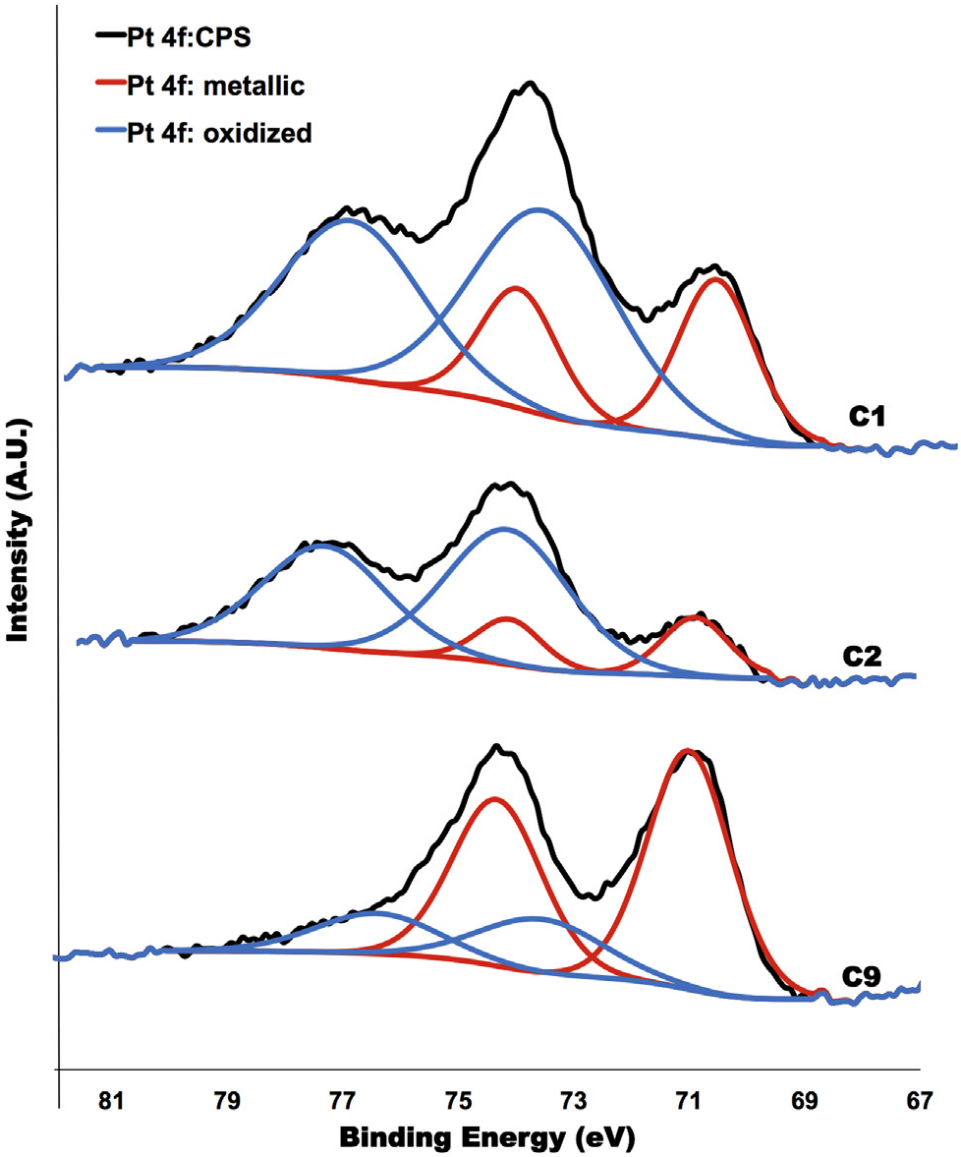

Figure 8: XPS spectra of platinum for the cathode CLs of cells 1, 2 and 9.

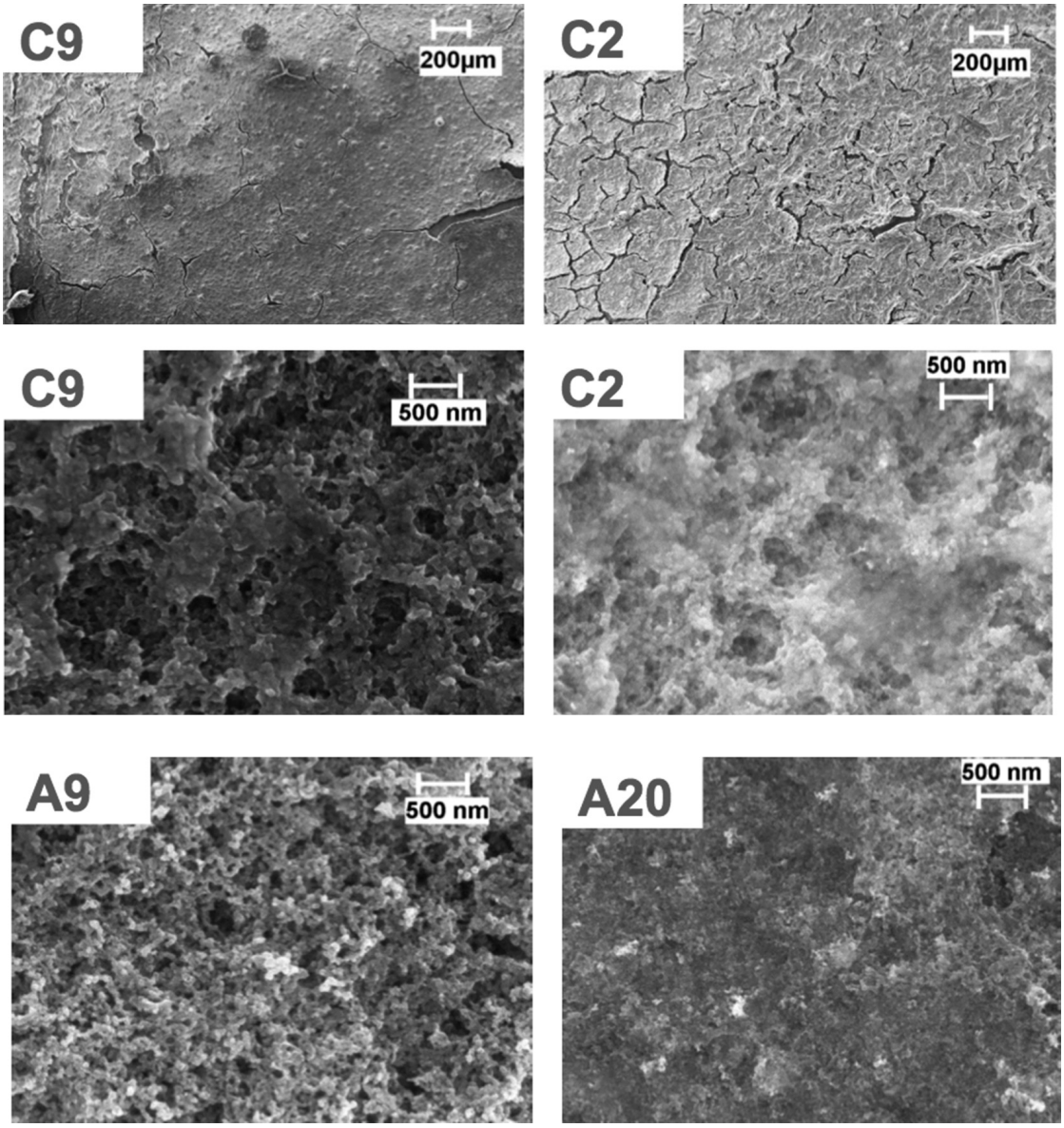

Figure 9: SEM images of the cathode catalyst surfaces of cells 2 and 9, and the anode catalyst surfaces 9 and 20. The secondary electron detector was used for this study.

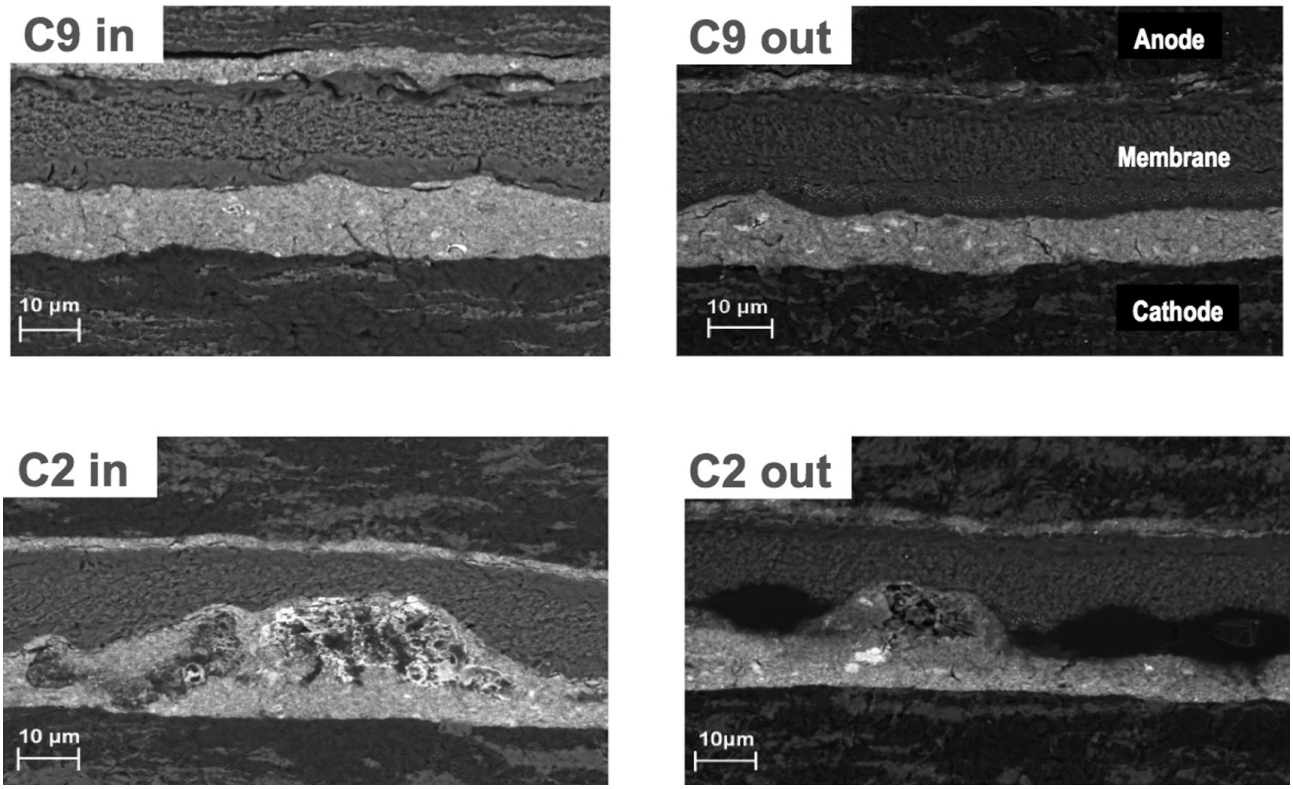

Figure 10: SEM images of the cut MEA samples close to the anode inlet and outlet of cells 2 and 9. The backscattered electron detector was used for this study.

TABLES

Table 1. Laboratory operating conditions during lifetime

Parameter	Units	Values
Current density	A cm^{-2}	0 - 0.35
Temperature	ºC	10 - 60
Reactant humidity anode	%	0 - 100
Reactant humidity cathode	%	10 - 100

Table 2. ECSA values obtained form CV relative to cell 9

Cell #	Anode [%]	Cathode [%]
1	+ 17	- 99
2	+ 12	- 95
9	+/- 0	+/- 0
10	+ 16	- 10
20	- 25	- 1

Table 3. Pt particle sizes in the CLs obtained from XRD

Cell #	Anode [nm]	Cathode [nm]
1	N/A	4.5 / 15.6
2	6.0	4.8 / 22.3
9	5.6	4.8
10	5.7	4.6
20	6.0	N/A